Theoretical study of interface structure and energetics in semicoherent Fe(001)/*MX*(001) systems (*M*=Sc, Ti, V, Cr, Zr, Nb, Hf, Ta; *X*=C or N)

Dan H. R. Fors and Göran Wahnström
Department of Applied Physics, Chalmers University of Technology, SE-412 96 Göteborg, Sweden
(Received 27 July 2010; published 5 November 2010)

We perform a systematic *ab initio* study of the electronic and atomic structure of semicoherent interfaces between bcc Fe and NaCl *MX* (*M*=Sc, Ti, V, Cr, Zr, Nb, Hf, Ta; *X*=C or N). The interface energetics is accessed by using a Peierls-Nabarro framework, in which *ab initio* data for the chemical interactions across the interface are combined with a continuum description to account for the elastic distortions. The key factors to the trends in the interface energy are identified and discussed with respect to the size of the misfit and the electronic structure of the *MX* phase. Our approach shows that the inclusion of lattice misfit can have a significant contribution to the interface energy (up to 1.5 J/m^2) and must therefore be thoroughly accounted for in the interface description. The results will have important bearings on our ability to understand and describe precipitate stability in steels.

DOI: 10.1103/PhysRevB.82.195410 PACS number(s): 68.35.−p, 61.72.Bb, 61.72.Lk, 71.15.Mb

I. INTRODUCTION

The abundance of solid-solid heterophase interfaces is an ubiquitous feature in advanced materials, which can have a decisive impact on the mechanical and other properties. In particular, the strength in metallic alloys is closely connected to the distribution of obstacles, such as precipitates and grain boundaries, which effectively hinder or block dislocation migration.[1] A fundamental understanding of the stability and energetics of the underlying interfaces of such structures is therefore an important step toward quantitative predictions of their impact on microstructure and properties of the material.[2]

In steel alloys, precipitation of secondary phases inside grains and at grain boundaries is commonly achieved by alloying additions of carbide and nitride formers, such as Ti, V, Cr, and Nb.[3] The interface structure of the precipitates has from experimental studies been found to depend on the size and chemical composition, and ranges from very small coherent VN (Ref. 4) platelets, via various-sized NbN (Ref. 5) and CrN (Ref. 6) particles, to larger semicoherent VN,[4,7,8] TiC,[9] and Nb(C,N) (Ref. 10) precipitates, where misfit dislocations are present at the interface. Still, the precise conditions for which the coherent or the semicoherent interface morphology occurs, in particular, inside grains, are not yet well established. Addressing this question calls for accurate data for the elastic constants, any lattice misfit between the precipitates and the matrix, and the interface energetics.

Accurate modeling of interfaces requires that the atomic and electronic structures can be described in a realistic manner. The nature of the chemical bonding at the interface can in general be highly complex and may simultaneously comprise ionic, covalent and metallic character. For real interfaces any mismatch between the structures of the two phases will also give rise to long-ranged stress fields surrounding the interface. This complexity therefore calls for methods that can bridge the different length scales and maintain an accurate description of the chemical interactions across the interface while simultaneously taking into account the extended elastic distortions.

In previous theoretical studies, interfaces between metals and carbides/nitrides have been investigated extensively by *ab initio* methods, where, in particular, density-functional-theory (DFT) calculations have proven to be a powerful and accurate tool to access the interface energetics, and to characterize the nature of the chemical bonding.[11–25] However, due to the extensive computational costs associated with these methods, a direct account for extended elastic distortions arising from lattice misfit have almost exclusively been prohibited. A semidirect approach to include the elastic displacements was explored in Refs. 24 and 25, where the elastic and chemical contributions for semicoherent and incoherent interfaces were approximated from *ab initio* simulations by using unit cells of moderate sizes, thereby ascertaining an accurate description of the interface interactions. However, the formulation of the interface energetics had the disadvantage of not providing a self-consistent description of the atomic structure and interactions across the interface. A promising alternative approach where the interface energetics is accessed in a self-consistent manner has been realized within a Peierls-Nabarro (PN) framework.[26–36] In the model, interface energetics is addressed by combining atomistic *ab initio* calculations for the chemical interactions with continuum theory to describe the elasticity of the materials. The framework has been applied to the metal-oxide Al/MgO,[32,33] the metal-nitride Fe/VN,[35,36] and the metal-metal NiAl/Mo (Ref. 34) interfaces and has shown potential for a proper interface description.

In the present paper we extend the work done in our previous studies[35,36] on the Fe/VN interface energetics. We perform a systematic investigation of the electronic and atomic structure of semicoherent interfaces between NaCl structured *MX* precipitates (*M*=transition metal; *X*=C or N) and bcc Fe, where the orientation relationship is given by the Baker-Nutting relation $(001)_{NaCl}\|(001)_{bcc}, [100]_{NaCl}\|[110]_{bcc}$. The chemical and elastic contributions to the semicoherent interface energetics are accounted for in a self-consistent manner within the Peierls-Nabarro framework. The former contribution is further thoroughly analyzed in order to identify the key factors to the trends of the chemical interactions across

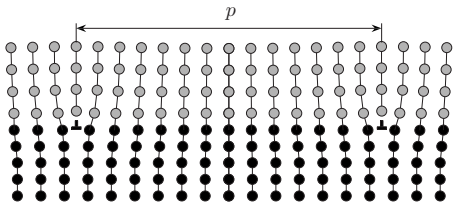

FIG. 1. Schematic figure of the semicoherent structure at the interface along the $\hat{x}$ direction. The misfit dislocations occur with the periodicity p. Black (gray) circles denote phase 1 (2).

the interface. Finally, we perform a comparison between the semicoherent and the coherent interface energetics of strained MX films in Fe with the aim to provide insights to the early stage of precipitation, its pathway and the precipitate morphology.

The paper is organized as follows. First, the semicoherent interface model is presented in Sec. II. Then, in Sec. III the computational techniques for the atomistic and continuum calculations are described followed by the results and discussion (Sec. IV). The main conclusions of our study are summarized in Sec. V.

II. SEMICOHERENT INTERFACE MODEL

In this paper we consider the sharp, planar interface between two semi-infinite crystals, (1) and (2), with the same (cubic) structure but with different lattice spacings, $a^{(1)}$ and $a^{(2)}$. The direction perpendicular to the interface is denoted with $\hat{z}$ and we assume $a^{(1)} > a^{(2)}$. The difference in the lattice spacings introduces a misfit f according to

$$f = 2\frac{a^{(1)} - a^{(2)}}{a^{(1)} + a^{(2)}}, \tag{1}$$

where we have used a symmetric definition[24] with respect to the two different phases.

Moderate misfit ($0 < f \lesssim 0.2$) will primarily be taken up periodically by formation of a square network of misfit dislocations arranged along the $\hat{x}$ and $\hat{y}$ directions. The formed semicoherent interface allows the majority of the atoms to achieve an optimal coherent configuration, except near the dislocation cores where the structure is highly distorted (cf. Fig. 1). The periodicity p of the dislocations is given by

$$p = \frac{a^{(1)}a^{(2)}}{a^{(1)} - a^{(2)}}. \tag{2}$$

In the discrete case the periodicity is restricted to $p = Pa^{(1)} = (P+1)a^{(2)}$ where P is an integer. We will assume p to be given by Eq. (2). For higher misfit the partial lattice matching at the interface will be lost and the interface becomes incoherent.

The semicoherent interface can be treated within an extended Peierls-Nabarro framework, where the total interface energy is decomposed into two terms

$$E_{\text{tot}} = E_{\text{chem}} + E_{\text{el}} \tag{3}$$

with E_{chem} describing the chemical energy originating from the breaking and creation of bonds in the formation of the interface and E_{el} the elastic energy arising from the atomic displacements. The chemical interactions across the interface are approximated by an effective two-dimensional (2D) potential energy surface, referred to as the γ surface, evaluated through atomistic *ab initio* calculations. The elastic distortions in the materials are accounted for by using a continuum description where the boundary conditions are derived by using the γ surface. The optimal atomic configuration and the corresponding interface energy are then obtained in a self-consistent manner by minimizing Eq. (3) with respect to the displacement fields. In the two following subsections we give a brief account of the above procedure for the semicoherent interface. For further details we refer to Ref. 36.

A. γ surface

The γ surface is determined through evaluation of the interface energy within a coherent interface approximation. The coherent interface system is constructed by straining the two phases in both the $\hat{x}$ and $\hat{y}$ directions into a common lattice parameters a in the interface plane. The parameter a is determined from linear elasticity theory and is chosen to minimize the sum of the elastic energy per volume for the two strained bulk phases, where the accompanying induced strains perpendicular to the interface (Poisson effect) are accounted for. The simultaneous straining of the two phases, rather than only adjusting one of the phases, is expected to give the best description of the chemical interactions across the interface, especially in the near coherent regions where the two phases will be close to satisfy the imposed strain condition.

The effective two-dimensional potential energy surface $\gamma(x,y)$ is then created by using a set of relative translations $\boldsymbol{\tau}$ of the two phases. At each specific translation the interface energy is minimized with respect to the interphase separation rather than utilizing one common separation for the entire interface. This approach is based on the results in our previous study of the Fe/VN interface,[35] where the elastic energy required to relax the interphase separation to its optimal distance was determined to be small. Furthermore, the minimization procedure with respect to the interphase separation is performed under the constraint that all mutual atomic distances in each respective phase are fixed, and hence, all further atomic relaxations are omitted. This constraint is imposed as a consequence of the dynamical instabilities found for the stoichiometric NaCl-structured VN, NbN, TaN, CrN, and CrC compounds.[37–39] These instabilities create large shear displacements in the NaCl-structure, which are stabilized first when metalloid vacancies are introduced. Therefore, in order to allow for a systematic study of all the MX compounds investigated in this work, we have decided to omit all atomic relaxations except for the minimization of the interphase separations. Finally, the acquired minima at the relative translations are interpolated by using a superposition of cosine functions, $\cos\frac{2\pi}{a}(mx+ny)(m,n \in \mathbb{Z})$, obeying the symmetry of the coherent interface.

We define the energy E_{coh} to be the minimum of the γ surface, corresponding to the interface energy of a fully coherent interface ($f=0$). We also define E_{incoh} to be the mean

of the γ surface, which is a measure of the interface energy for an incoherent (in both the $\hat{x}$ and $\hat{y}$ directions) structure. The interface energy for the semicoherent interface will be bounded by E_{coh} and E_{incoh}.

B. Peierls-Nabarro framework

The atomic distortions for a periodic array of misfit dislocations at a semicoherent interface between two semi-infinite crystals, (1) and (2), can be accounted for in the Peierls-Nabarro framework. The elastic response of the two crystals is assumed to be described by linear elasticity theory and the discrete atomic nature of the crystals is thus replaced by two continuum media with two different sets of elastic constants. The misfit dislocations are assumed to be of pure edge type with the Burger's vectors parallel to $\hat{x}$. For an edge dislocation the displacements of the elastic media just below or above the interface, $u^{(1)}(x)$ and $u^{(2)}(x)$, will lie only along the $\hat{x}$ direction. The relative displacement parallel to the interface is denoted with $u(x)=u^{(1)}(x)-u^{(2)}(x)$ while the relative displacement perpendicular to the interface is set to zero. The displacements are all functions of the periodicity p, and we impose the boundary conditions $u(-p/2)=u(p/2)=0$.

Assuming continuity of the stress field across the interface, the elastic energy per unit area is a functional $E_{\mathrm{el}}^{\mathrm{edge}}=E_{\mathrm{el}}^{\mathrm{edge}}[u(x)]$ of the displacement field $u(x)$, despite the difference in the elastic constants. For a periodic array of edge dislocations we have

$$E_{\mathrm{el}}^{\mathrm{edge}}[u(x)] = -\frac{K_e}{4\pi p}\int_{-p/2}^{p/2}\int_{-p/2}^{p/2}\ln\left|\sin\frac{\pi}{p}(x-x')\right|\frac{du(x')}{dx'}\frac{du(x)}{dx}dx'dx, \tag{4}$$

where the energy coefficient K_e can be evaluated with knowledge of the elastic constants and the orientation of the crystals.

The chemical energy per unit area is given by an integral over the γ surface according to

$$E_{\mathrm{chem}}^{\mathrm{edge}}[u(x)] = \frac{1}{p}\int_{-p/2}^{p/2}\gamma[U(x)]dx, \tag{5}$$

where $U(x)=\frac{a}{2}+\frac{a}{p}x+u(x)$ is the disregistry across the interface. The integrand $\gamma[U(x)]$ here refers to the one-dimensional (1D) cut, parallel to the $\hat{x}$ direction, in the two-dimensional effective potential energy surface that gives the lowest mean energy when integrated along the corresponding line. Finally, the total interface energy for the system is obtained by minimizing

$$E_{\mathrm{tot}}^{\mathrm{edge}}[u(x)] = E_{\mathrm{chem}}^{\mathrm{edge}}[u(x)] + E_{\mathrm{el}}^{\mathrm{edge}}[u(x)] \tag{6}$$

with respect to $u(x)$. By taking the functional derivative of Eq. (6) with respect to $u(x)$, the usual PN integrodifferential equation is obtained.

In order to account for the full square dislocation network exemplified in this paper, the 1D solution is subsequently transferred to 2D according to

$$E_{\mathrm{tot}} = 2E_{\mathrm{el}}^{\mathrm{edge}} + 2(E_{\mathrm{chem}}^{\mathrm{edge}} - E_{\mathrm{coh}}) + E_{\mathrm{coh}}. \tag{7}$$

We have here assumed that perpendicular dislocations at the interface do not interact. This assumption has in our previous study[36] been shown to be a valid approximation for the Fe/VN interface.

III. COMPUTATIONAL DETAILS

A. Atomistic modeling

The atomistic calculations are performed within the framework of DFT as implemented in the Vienna *ab initio* simulation package (VASP).[40–42] The exchange-correlation functional is treated with the spin-polarized generalized gradient approximation according to Perdew and Wang[43] (PW91) for the systems with $M \neq$ Nb, Cr and according to Perdew-Burke-Ernzerhof[44] (PBE) for the systems with M =Nb, Cr.[45] Blöchl's projector-augumented-wave formalism as implemented by Kresse and Joubert[46] is employed for the electron-ion interaction. The standard Fe, C, and N potentials with eight, four, and five valence electrons are used while the semicore electrons are included as valence electrons for the M atoms where available. The k-point integration over the Brillouin zone is performed by using a Monkhorst-Pack grid and the first-order Methfessel-Paxton smearing scheme with a fictitious temperature broadening of 0.1 eV. The plane-wave cutoff energy is chosen in the range 450–700 eV, dependent on the specific system, in order to ensure that the total energies are converged to within a few millielectron volt per atom.

The similarities and differences in the electronic structure for the considered systems are studied in terms of charge transfers between different constituents, real-space electron charge densities, and atom-projected density of states (DOSs). The charge transfers are quantified through Bader analysis[47] based on the approach given in Ref. 48. The Bader scheme represents an intuitive way to separate atoms from each other in compounds, based solely on the charge density, and can provide value information about charge redistributions. The third root of the ratio between the Bader volumes associated with each atom in the bulk phases is also utilized to define the ratio between the projection radii used for the evaluation of the atom-projected DOSs in the MX compounds. The projection spheres are then made as large as possible without overlap between neighboring spheres. For the Fe phase the projection radius is set to 1.0 Å.

1. Bulk properties

All of the considered transition metal carbides and nitrides in this paper are confined to an ideal stoichiometric sodium chloride structure. The presence of nonmetal vacancies, which experimentally are known to stabilize the NaCl-structure for many of the MX phases, are thus omitted in order to reduce the number of varying parameters when performing the trend study. Furthermore, the MX's in the groups III-V are known to adopt a nonmagnetic configuration while for consecutive compounds such as CrN and FeN magnetic ordering becomes important.[49–51] Therefore, we investigate the stability of the nonmagnetic and the ferromagnetic state

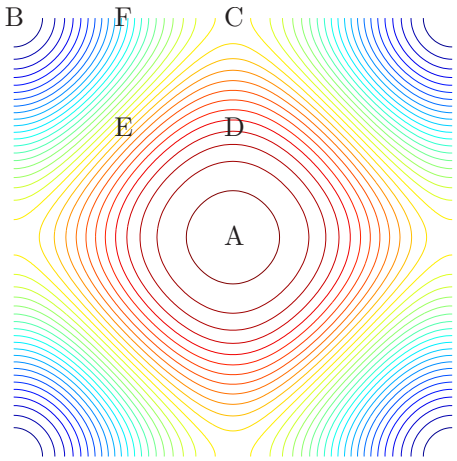

FIG. 2. (Color online) The γ surface of the Fe/TiC interface. Consecutive contour lines differ by 0.1 $\mathrm{J/m^2}$. The maximum of the γ surface lies in the middle (corresponding to Fe on top Ti) and the minimum lies in the corner (corresponding to Fe on top C).

for all the *MX*'s. In addition, for the CrX and FeX phases three antiferromagnetic states are considered corresponding to two single layer configurations $(\uparrow\downarrow\uparrow\downarrow\ldots)$ along the $[110]_{\mathrm{NaCl}}$ and the $[111]_{\mathrm{NaCl}}$ direction, respectively, and one double layer structure $(\uparrow\uparrow\downarrow\downarrow\ldots)$ along the $[110]_{\mathrm{NaCl}}$ direction.

The lattice constants d, the bulk moduli B, and the elastic constants c_{11}, c_{12}, and c_{44} for the Fe phase and the *MX* compounds are determined by following the procedure in Ref. 52: (i) an isotropic strain gives d and $B=(c_{11}+c_{12})/3$ from a Birch fit of at least third order, and (ii) volume-conserving orthorhombic and monoclinic strains give $c_{11}-c_{12}$ and c_{44}, respectively, from polynomial fits. For the Baker-Nutting orientation relationship the lattice constants d are then related to the interface parameters according to $a^{\mathrm{Fe}}=d^{\mathrm{Fe}}$ and $a^{MX}=d^{MX}/\sqrt{2}$. The calculations are performed by using a cubic unit cell $(d\times d\times d)$ and a k-point grid consisting of at least $10\times10\times10$ points.

2. Interface properties

The γ surface is determined through evaluation of the interface energy within a coherent interface approximation for six relative translation vectors (A-F) of the two phases, cf. Fig. 2. Each coherent interface system is represented by using a computational unit cell containing a standard slab geometry with n_{Fe} expanded Fe layers on top of n_{MX} compressed *MX* layers. The interlayer distances perpendicular to the interface in the two respective phases are adjusted to account for the Poisson relaxation. The cell is subject to periodic boundary conditions in all three directions. Each *MX* $(M\neq\mathrm{Cr})$ layer contains one *M* atom and one *X* atom while each Fe layer corresponds to one Fe atom. The CrX systems are composed of twice the number of atoms in each layer in order to also allow for the antiferromagnetic spin structures. The converged k-point grids are set to at least $10\times10\times1$ $(12\times6\times1)$ points for the $M\neq\mathrm{Cr}(M=\mathrm{Cr})$ systems.

At $T=0$ K the interface energy can for each relative translation $\boldsymbol{\tau}$ be evaluated according to

$$\gamma(\boldsymbol{\tau}) = \min_{z_{\mathrm{sep}}} \frac{E_{\mathrm{Fe}/MX}(\boldsymbol{\tau}, z_{\mathrm{sep}}) - \sum_i \mu_i N_i}{2A}, \tag{8}$$

where A is the area, N_i the number of atoms for the constituent i, and $E_{\mathrm{Fe}/MX}(\boldsymbol{\tau}, z_{\mathrm{sep}})$ is the internal energy of the coherent interface system at the interphase separation z_{sep}. The factor 2 in the denominator is included to account for the presence of two surfaces in the computational unit cell. The chemical potentials μ_i are evaluated through separate calculations for the strained stoichiometric bulk phases.

Convergence tests with respect to the number of layers show that a setup with $n_{\mathrm{Fe}}=5$ and $n_{MX}=5$ is sufficient to reduce the interface energy error from the artificial interface interactions through the slabs, originating from the finite size of the computational unit cell, to less than 0.03 $\mathrm{J/m^2}$. This layer configuration is therefore utilized for all of the interface systems. The equal parity for n_{Fe} and n_{MX} is here imposed in order to create two identical interfaces within the cell.

The absolute bond strength of the interface system is analyzed in terms of the work of separation W_{sep}, i.e., the reversible work required to separate the interface into two free surfaces while neglecting diffusional and plastic degrees of freedom.[53] By denoting the surface energies of the free Fe and *MX* surfaces with σ_{Fe} and σ_{MX}, respectively, the work of separation at each specific relative translation can be expressed as

$$W_{\mathrm{sep}}(\boldsymbol{\tau}) = \sigma_{\mathrm{Fe}} + \sigma_{MX} - \gamma(\boldsymbol{\tau}), \tag{9}$$

where the free surfaces are restricted to the same strains as for the corresponding interface system. The surface energy σ for each phase is calculated according to

$$\sigma(n) = \frac{E_{\mathrm{surf}}(n) - \sum_i \mu_i N_i}{2A}, \tag{10}$$

where $E_{\mathrm{surf}}(n)$ is the internal energy of a surface system represented by a standard slab geometry with n layers and a 12 Å thick vacuum region. The chemical potentials μ_i for the stoichiometric bulk phase are obtained from an arithmetic average over the increments $\Delta E_{\mathrm{surf}}=E_{\mathrm{surf}}(n)-E_{\mathrm{surf}}(n-1)$ in the region with sufficiently large n values. This evaluation procedure achieves a fast convergence to a stable value for the surface energy and avoids the linear divergence with respect to n that can arise if μ_i instead would be obtained from independent bulk calculations.[54,55] Convergence tests with respect to the number of layers show that $n_{\mathrm{Fe}}=16$ and $n_{MX}\in[8,16]$ are sufficient to reduce the surface energy error to less than 0.01 $\mathrm{J/m^2}$.

B. Continuum modeling

The minimization of the total energy functional in Eq. (6) is performed numerically. We define $u(x)$ as a piece-wise linear function with the values u_i at the nodal points x_i making du/dx constant between the points. The nonlinear equations

TABLE I. Calculated lattice parameters (d), bulk moduli (B), elastic constants (c_{11}, c_{12}, c_{44}), and cohesive energies E_C for the Fe and the MX bulk phases. The corresponding experimental values are given in parentheses. For the MX's the Bader charge transfers from M to X atoms (Bader) are also given. The cohesive energies are evaluated with respect to the spin-polarized broken-symmetry states of the isolated atoms.

	d (Å)	B (GPa)	c_{11} (GPa)	c_{12} (GPa)	c_{44} (GPa)	Bader ($\|e\|$/atom)	E_C (eV/formula unit)
Fe (PW91)	2.831 (2.866)[a]	175	258	133	94		5.00 (4.28)[b]
Fe (PBE)	2.835 (2.866)[a]	175	258	133	94		4.94 (4.28)[b]
ScC	4.684 (4.720)[c]	153	304	77	61	1.62	12.56 (12.74)[c]
TiC	4.336 (4.328)[d]	248	508	118	168	1.63	14.92 (14.32)[c]
VC	4.160 (4.159)[d]	311	645	145	183	1.45	14.08 (13.88)[c]
CrC	4.106 (4.117)[e]	262	501	142	89	1.35	11.68 (11.59)[e]
FeC	4.000 (4.085)[e]					1.23	11.80 (11.35)[e]
ZrC	4.723 (4.698)[d]	219	454	102	150	1.84	15.79 (15.86)[f]
NbC	4.507 (4.469)[d]	298	642	127	163	1.75	15.88 (16.52)[f]
HfC	4.645 (4.636)[d]	237	507	102	171	2.04	16.34 (16.22)[g]
TaC	4.484 (4.455)[d]	322	718	124	179	1.97	17.27 (17.12)[g]
ScN	4.522 (4.509)[c]	200	388	107	166	1.77	13.35 (13.44)[c]
TiN	4.255 (4.240)[d]	273	574	123	164	1.70	13.99 (13.39)[c]
VN	4.125 (4.126)[d]	330	633	179	135	1.57	12.48 (12.49)[c]
CrN	4.144 (4.149)[e]	247	505	118	134	1.48	10.09 (10.29)[e]
FeN	4.085 (4.133)[e]					1.49	9.72 (9.17)[e]
ZrN	4.620 (4.567)[d]	248	522	112	112	1.83	14.78 (15.05)[f]
NbN	4.456 (4.379)[h]	304	618	147	81	1.72	13.90 (14.99)[f]
HfN	4.539 (4.520)[d]	270	588	112	124	2.00	15.20 (15.24)[g]
TaN	4.427 (4.336)[d]	328	685	149	64	1.80	15.05 (15.27)[g]

[a]Experimental data from Ref. 56.
[b]Experimental data from Ref. 57.
[c]Experimental data from Ref. 58.
[d]Experimental data from Ref. 59.
[e]Estimated value based on thermodynamical data, from Ref. 58.
[f]Experimental data from Ref. 60.
[g]Experimental data from Ref. 61.
[h]Experimental data from Ref. 62.

$$\frac{\partial E_{\text{tot}}^{\text{edge}}}{\partial u_i} = 0, \quad \forall\, i \tag{11}$$

are then solved by using a conjugate-gradient algorithm. The number of nodal points is chosen to make the total energy converge within 10^{-3} J/m^2.

IV. RESULTS AND DISCUSSION

A. Bulk properties

In Table I and Fig. 3 we present the calculated lattice parameters, the bulk moduli, the elastic constants, the cohesive energies E_C, and the charge transfers for the investigated bulk MX's. In addition, partial data for FeN and FeC are also given. The magnetic structure at the equilibrium volume is determined to be ferromagnetic for Fe, CrC, and FeN, single layer antiferromagnetic along the $[110]_{\text{NaCl}}$ direction for CrN, and nonmagnetic for the remaining systems. The calculated lattice parameters are found to be in reasonable agreement with experimental data with deviations smaller than 2.1%. The values and trends are also consistent with previous theoretical investigations.[49,63,64] For the cohesive energies a qualitative agreement with experimental values is obtained, although the relative deviations are larger than for the lattice constants. However, it should be noted that the MX phases in general are substoichiometric with respect to X, which is known to have a sizable effect on the bonds in the material[65] and hence, a direct comparison with experimental data should be done with a little caution.

The properties of the bulk MX's and their respective trends with respect to substitution of the M or the X atom have been studied extensively with a large variety of theoretical and experimental methods.[58,60,61,64–71] The bonding in the compounds has been determined as a mixture of covalent, ionic, and metallic contributions, which are associated with (i) the hybridization between the M and X atoms, leading to formation of bonding and antibonding pd states, (ii) the charge transfer from the M atom to the X atom, and (iii) the hybridization between the M atoms.[66,67,69] In addition,

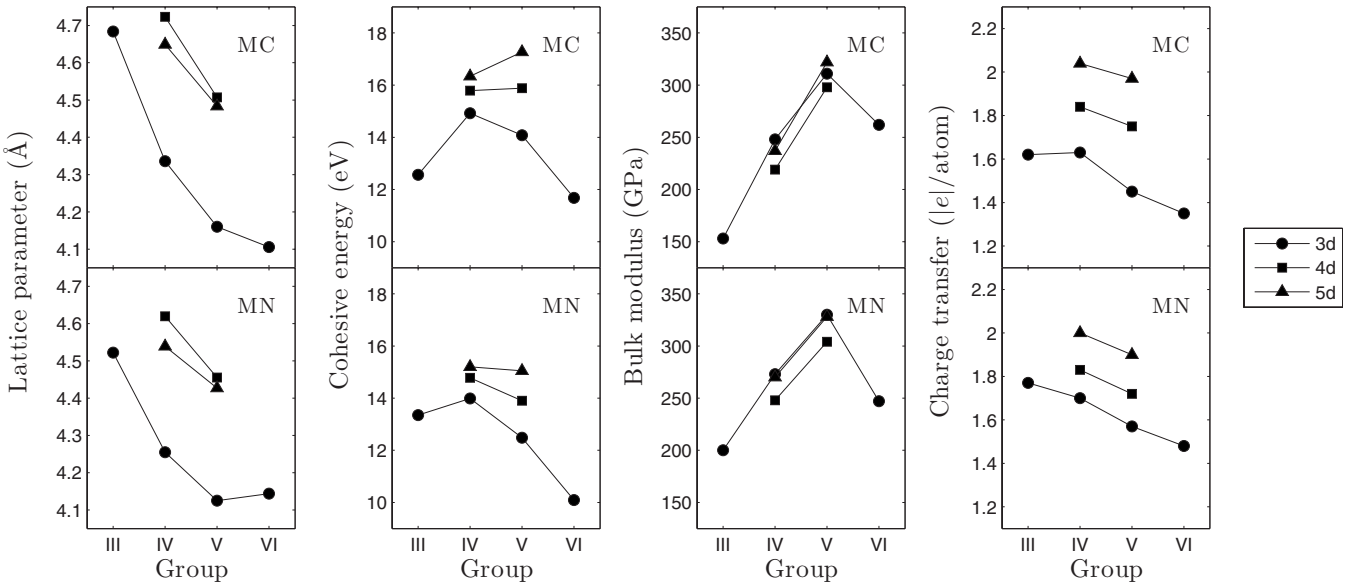

FIG. 3. Variations in, from left to right, the lattice parameters, the cohesive energies, the bulk moduli, and the charge transfers of the investigated 3*d*, 4*d*, and 5*d* *MX*'s as a function of the parent *M* group.

theoretical studies have also demonstrated the presence of non-neglectable bond contributions from *X*-*X* interactions.[64,71] The formed electronic structure is similar for all the *MX* compounds (cf. Fig. 4) and consists of (i) a lower valence band (LVB) with mainly *X* 2*s* states, (ii) an upper valence band (UVB) with a mixture of bonding *X* 2*p* and *M d* states, and (iii) a conduction band (CB) containing antibonding and nonbonding states with mainly *M d* character.

The similarity in the electronic structure for all the *MX*'s in combination with the distinct separation between the regions with the bonding and the antibonding states provide a qualitative understanding of bond strength variations in terms of band filling arguments.[65,67,69] Within a rigid band model the largest cohesive energy along a transition metal period in the periodic table is expected when the bonding states in the UVB band are completely filled and the antibonding states in the CB band are empty. According to this picture the maximum bond strength occurs in group IV for the carbides and in group III for the nitrides. Removing (adding) electrons from (to) the system will deplete (fill) the bonding (antibonding) states and the bond strength will consequently decrease.

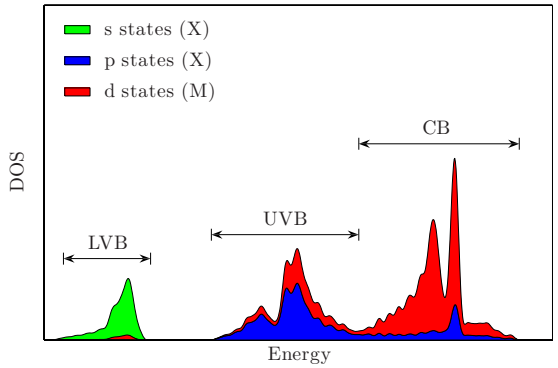

FIG. 4. (Color online) A schematic picture of the electronic structure of the *MX* phases, showing the orbital projected density of states (DOS) for the lower and upper valence band (LVB and UVB) and for the conduction band (CB). The states are superpositioned on each other in such a way that the upper envelope corresponds to the summation of the states.

Our calculated cohesive energies are consistent with the rigid band model with the exceptions that the value for ScN is lower than expected and that the maximum values for the 4*d* and 5*d* MC's are shifted to group V instead of occurring in group IV. Presumably, the explanation for these deviations is the previous finding[61,69] that the rigid band assumption is only valid for qualitative and not quantitative trends predictions. Care should therefore be taken to not rely on band filling arguments alone. Finally, we note that the trends of the charge transfers and the monotonic increase in the cohesive energy when down going a group are in agreement with previous predictions based on hybridization in a two-level model consisting of the atomic *M d* and the *X* 2*p* energy levels.[64]

B. Interface properties

In Table II we summarize the common lattice parameters and strains for the coherent Fe/*MX* interface systems. The former are, as expected from the elastic constants, closer to the more rigid *MX* phase and the largest strains thus occur in the Fe phase.

1. Coherent interface energies

The interface energies at the six translational sites (A-F) for the considered systems are presented in Table III and in Fig. 5 as a function of the *M* atom. The effective potential energy surfaces are characterized by three essential features: (i) there is a large difference in the interface energy (1.5–2 eV/a^2) between the optimal (site B) and the least

TABLE II. Calculated misfit (f), energy coefficient (K_e), perpendicular and parallel strains ($\epsilon_\perp$, $\epsilon_\parallel$), common lattice parameter (a) and periodicity of the misfit dislocations (p) for the investigated Fe/MC (Fe/MN) interface systems.

	f (%)	K_e (GPa)	$\epsilon_\perp^{\mathrm{Fe}}$ (%)	$\epsilon_\parallel^{\mathrm{Fe}}$ (%)	$\epsilon_\perp^{MX}$ (%)	$\epsilon_\parallel^{MX}$ (%)	a (Å)	p (Å)
Fe/ScX	15.7 (12.2)	106 (141)	−10.1 (−8.4)	9.8 (8.2)	3.1 (2.3)	−6.2 (−4.2)	3.107 (3.063)	19.5 (24.7)
Fe/TiX	8.0 (6.1)	147 (150)	−5.9 (−4.6)	5.7 (4.5)	1.1 (0.7)	−2.4 (−1.7)	2.993 (2.956)	37.0 (48.0)
Fe/VX	3.8 (3.0)	156 (148)	−3.0 (−2.3)	2.9 (2.2)	0.4 (0.4)	−1.0 (−0.8)	2.913 (2.894)	75.3 (96.5)
Fe/CrX	2.4 (3.3)	125 (143)	−1.7 (−2.4)	1.6 (2.3)	0.4 (0.4)	−0.7 (−1.0)	2.881 (2.901)	120.9 (87.4)
Fe/ZrX	16.5 (14.3)	141 (137)	−12.4 (−11.1)	12.0 (10.7)	2.3 (1.7)	−5.1 (−4.0)	3.171 (3.135)	18.6 (21.2)
Fe/NbX	11.7 (10.6)	152 (133)	−9.6 (−8.4)	9.1 (8.2)	1.1 (1.3)	−2.9 (−2.7)	3.094 (3.066)	25.7 (28.3)
Fe/HfX	14.9 (12.5)	147 (143)	−11.5 (−10.0)	11.1 (9.7)	1.7 (1.2)	−4.3 (−3.3)	3.146 (3.104)	20.4 (24.0)
Fe/TaX	11.3 (10.0)	157 (130)	−9.4 (−8.2)	9.1 (8.0)	0.9 (1.0)	−2.6 (−2.4)	3.088 (3.056)	26.5 (29.6)

favorable (site A) position at the interface, (ii) the trend along a period is similar for all translational sites, and (iii) the trend along the 3d period is different for carbides and nitrides with in particular a substantial change in the interface energy for the Fe/ScC system. Furthermore, we note that the interface energy at site B is negative for many of the MX's, and the formed bonds across the interface are hence stronger than in the corresponding bulk phases.

2. Work of separation and surface energies

The trends for the work of separation at the minimum and maximum position at the γ surface, Fe on top X and Fe on top M, respectively, are shown in Fig. 6 together with the trends for the Fe(001) and MX(001) surface energies.

The obtained surface energies for the Fe systems are in agreement with previous experimental and theoretical studies.[72] We also find that the energies have a very weak strain dependence, where the energy cost per Fe atom increases only slowly with higher misfit. Still, the dependence indicates that the lateral bonds in the $\hat{z}$ direction become more important for the bond strength in the bulk phase as the strains grow larger.

For the MX surfaces the differences along a period show a clear correlation between the surface energies and the cohesive energies (cf. Fig. 3), where the maxima of the quantities coincide at the same groups. (It should here be pointed out that although the imposed strains decrease the bond strength in the bulk MX's to a certain extent as compared to unstrained phases (<0.3 eV per formula unit), the trends for E_C are qualitatively unchanged.) The connection to the cohesive energies can be understood in terms of a simple nearest-neighbor broken-bond scheme and as a consequence the same band filling arguments as for the bulk MX's can be applied to account for the surface energy trends.[73–75]

The trends of the work of separation are found to partially inherit the trends of the interface energies. However, the magnitude of the variations along a period in the former are reduced compared to the latter due to a cancellation from the MX's surface energies. From the results we find that the absolute interface bond strength are characterized by three general features: (i) the interface bonds at site B are much stronger than at site A, (ii) the bond strength increases along a period, and (iii) the interface bonds in the Fe/ScC system at site B are significantly stronger than for the remaining 3d MC's. Note that only the first feature can with certainty be concluded from the interface energies since it is the only feature where the effect of the surface energies cancels out. The above trends can be understood on the basis of charge density distributions and band filling arguments for the interface and surface systems, and are discussed in the following subsections.

TABLE III. Calculated values of the γ surface at the six translation states A-F for the investigated Fe/MC (Fe/MN) interface systems.

	A (eV/a^2)	B/E_{coh} (eV/a^2)	C (eV/a^2)	D (eV/a^2)	E (eV/a^2)	F (eV/a^2)	E_{incoh} (eV/a^2)
Fe/ScX	1.77 (1.93)	−0.47 (0.43)	0.98 (1.65)	1.54 (1.87)	1.10 (1.69)	0.35 (1.13)	0.93 (1.52)
Fe/TiX	2.09 (1.79)	0.22 (0.22)	1.42 (1.44)	1.89 (1.67)	1.45 (1.36)	0.86 (0.81)	1.36 (1.26)
Fe/VX	1.68 (1.46)	−0.04 (−0.03)	1.00 (1.04)	1.44 (1.31)	1.02 (0.98)	0.49 (0.46)	0.95 (0.90)
Fe/CrX	1.40 (1.42)	−0.16 (−0.01)	0.76 (0.93)	1.19 (1.25)	0.87 (0.97)	0.33 (0.45)	0.76 (0.85)
Fe/ZrX	2.20 (1.67)	0.12 (0.06)	1.56 (1.40)	2.01 (1.57)	1.59 (1.33)	0.95 (0.81)	1.46 (1.20)
Fe/NbX	1.83 (1.36)	−0.13 (−0.18)	1.28 (1.06)	1.63 (1.24)	1.23 (0.97)	0.60 (0.44)	1.12 (0.86)
Fe/HfX	2.26 (1.61)	0.19 (0.06)	1.59 (1.35)	2.06 (1.52)	1.64 (1.28)	0.98 (0.78)	1.51 (1.15)
Fe/TaX	1.77 (1.15)	−0.11 (−0.23)	1.20 (0.90)	1.58 (1.06)	1.18 (0.82)	0.54 (0.33)	1.07 (0.71)

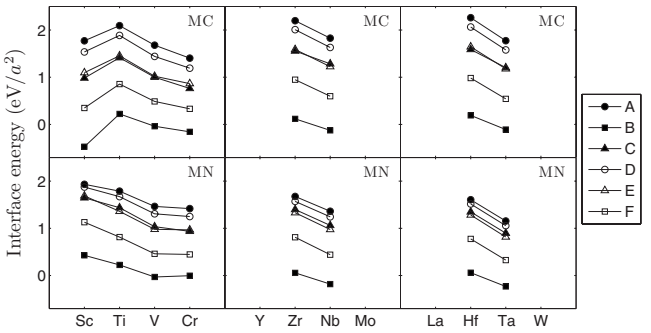

FIG. 5. Variations in the γ surfaces at the six relative translations (A-F) for the investigated Fe/MX interfaces with respect to the M atom.

3. Site dependence of the interfacial bond strength

The real-space electron charge-density and the induced charge density compared to the free surfaces at site B and at site A for the investigated Fe/MC 3d interface systems are shown in Figs. 7 and 8, respectively. Furthermore, the atom-projected DOSs for the corresponding bulk, surface and interface systems are presented in Fig. 9.

The real-space analysis reveals a high charge density between the Fe and the C interface atoms at site B, which is even higher than the charge density between the M and the C atoms in the MC phase. In contrast, at site A this feature is essentially absent and the optimal interphase separations are noticeably larger. Further, the induced charge densities at the two sites are also found to be rather different. At site B there is pronounced charge transfer from the Fe to the C atoms, indicating a partial ionic bond whereas at site A the charge redistributions are symmetrically localized around the center of the interstitial region between the Fe and M atoms. The higher charge depletion of the Fe phase at site B is confirmed by a comparison of the Bader charges between the interfaces and the free surfaces, see Fig. 10. The Bader analysis also reveals that (i) the charge redistributions occur mainly in the layers closest to the interface, (ii) the magnitude of the charge transfers range up to the order of one sixth of the total transfer in bulk FeC (cf. the coordination number of the NaCl-structure being six), and (iii) charge transfer occurs to both the C and the M atoms at site B.

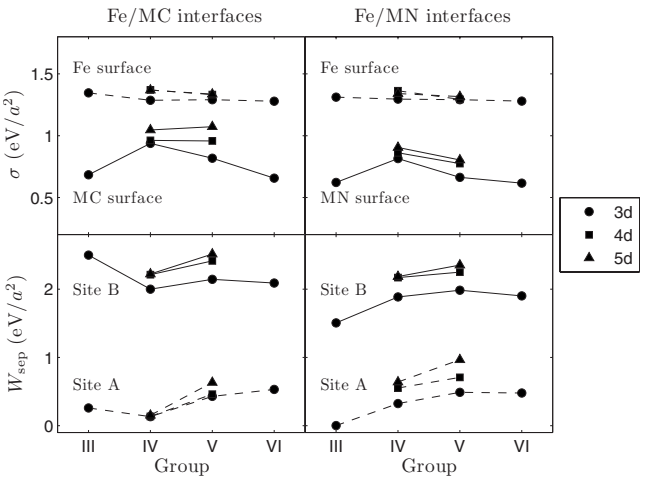

FIG. 6. The upper (lower) panel shows the variation in the surface energy (work of separation) for the investigated Fe/MX interface systems as a function of the parent M group.

The atom-projected DOSs are found to have very similar character for all systems. The results show that the electronic structure of the strained bulk MC's follows the rigid band picture with the LVB, the UVB and the CB gradually shifted downwards in energy as the filling increases. The bulk Fe states on the other hand emerge as almost strain independent with only small variations along the period. As the free surfaces are created the LVB and the UVB for the MC's are shifted upwards in energy while for the Fe phase states below and above the Fermi level are displaced downwards in energy. The upwards shift of the UVB for the MC's decreases the separation compared to the CB region, which can be interpreted as a reduction in the hybridization between the C 2p and the M 3d states due to the change in the coordination number for the surface atoms.

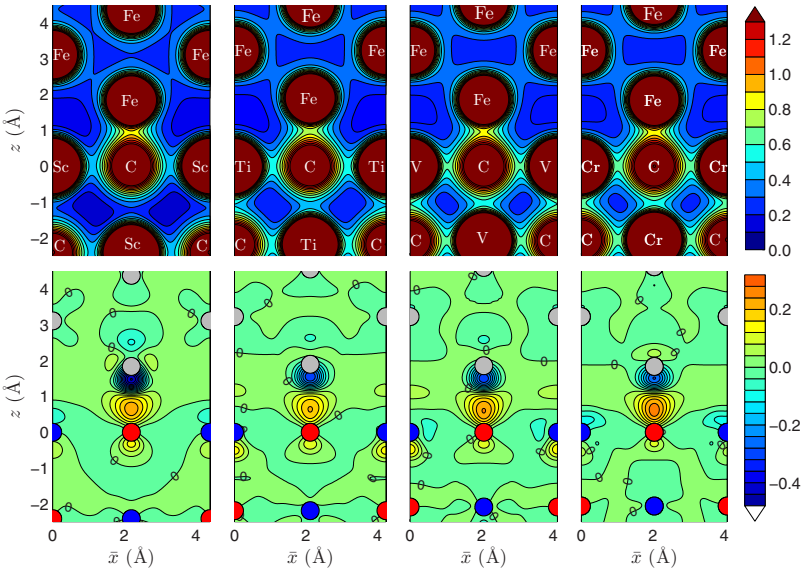

FIG. 7. (Color online) The upper (lower) panel shows the valence-electron density (induced valence-electron density compared to the free surfaces) at the minimum of the γ surface for the investigated 3d Fe/MC interfaces. The structure is viewed along the $(100)_{\mathrm{NaCl}}$ plane with $\bar{x}$ running from 0 to $\sqrt{2}a$. The consecutive contours change by 0.1 (0.04) electrons/Å^3. In the lower panel negative (positive) values denote charge depletion (accumulation), and the filled circles denote the center positions of the atoms.

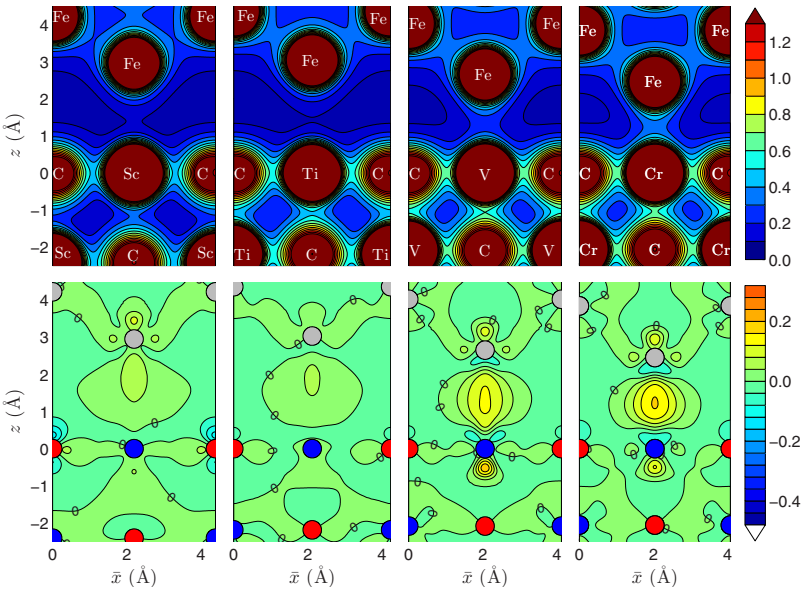

FIG. 8. (Color online) The upper (lower) panel shows the valence-electron density (induced valence-electron density compared to the free surfaces) at the maximum of the γ surface for the investigated 3*d* Fe/MC interfaces. The structure is viewed along the $(100)_{\mathrm{NaCl}}$ plane with $\bar{x}$ running from 0 to $\sqrt{2}a$. The consecutive contours change by 0.1 (0.04) electrons/Å^3. In the lower panel negative (positive) values denote charge depletion (accumulation), and the filled circles denote the center positions of the atoms.

The site dependence of the work of separation can now be understood from a comparison between the surface and the interface DOSs together with the results from the real-space analysis. For the interface systems with $M \neq \mathrm{Sc}$ (the $M = \mathrm{Sc}$ case is discussed in Sec. IV B 5) the redistributions of states at site B are found to reverse the majority of states that are shifted due to the surface cleavage. Consequently, the strength of the hybridization between the *M* 3*d* and the C 2*p* states is restored and the states in the Fe phase are recreated. Based on that the shifted states in the Fe phase correlate to the bonds in the lateral direction, the latter supports formation of metallic Fe-*M* bonds across the interface, which compensates for the broken Fe-Fe and *M*-*M* bonds. Effectively, we can thus conclude that the Fe phase at site B acts as a natural extension of the *MX* phase, where the chemical environment has contributions of ionic, covalent, and metallic character. In contrast, none of the above restoration of the bulk states are found to occur at site A and the interface bonds are therefore much weaker than for site B.

Finally, analyzes of the electron structure of the remaining four relative translations C-F (not included) show that the interface bond strength at these intermediate sites can be ex-

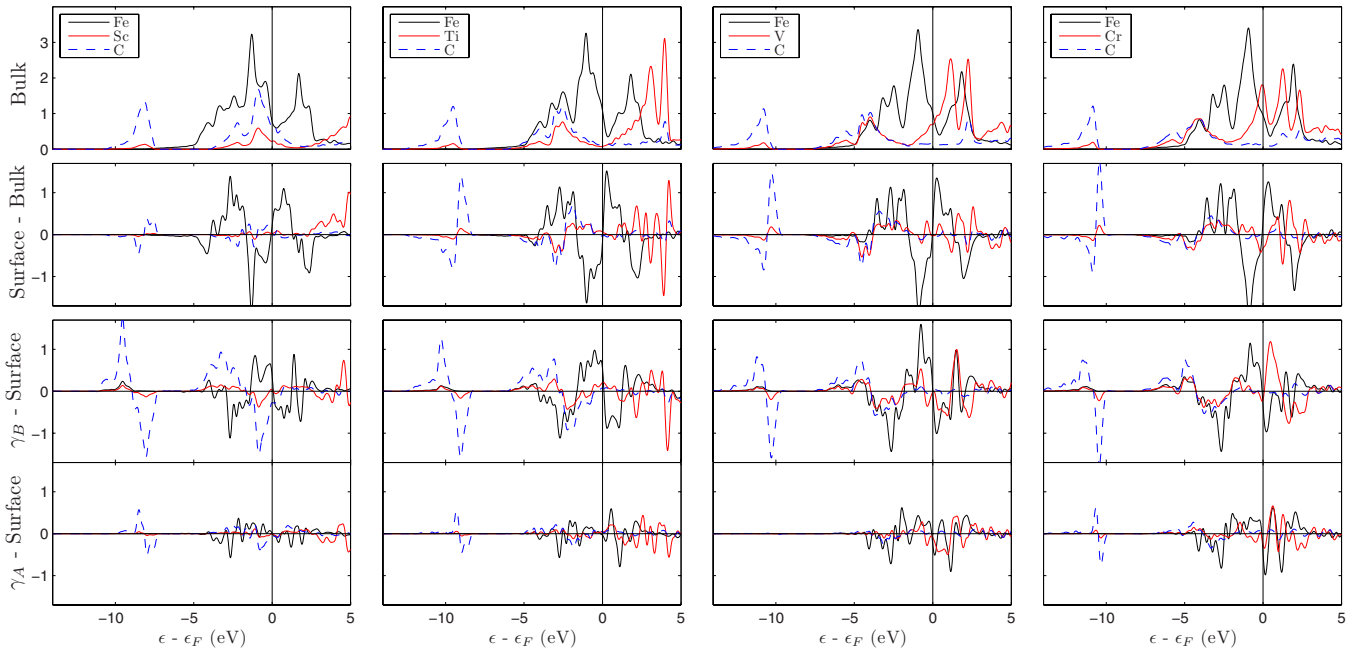

FIG. 9. (Color online) The top panel shows the atom-projected DOSs for the Fe and the 3*d* MC bulk systems. The remaining three panels show, from top to bottom, the difference (ΔDOS) between the surface and the bulk DOSs for the first surface layer, the difference between the optimal interface configuration (Fe on top C) and the surface DOSs for the first interface layer, and the difference between the least favorable interface configuration (Fe on top M) and the surface DOSs for the first interface layer. A positive (negative) ΔDOS corresponds to creation (depletion) of states.

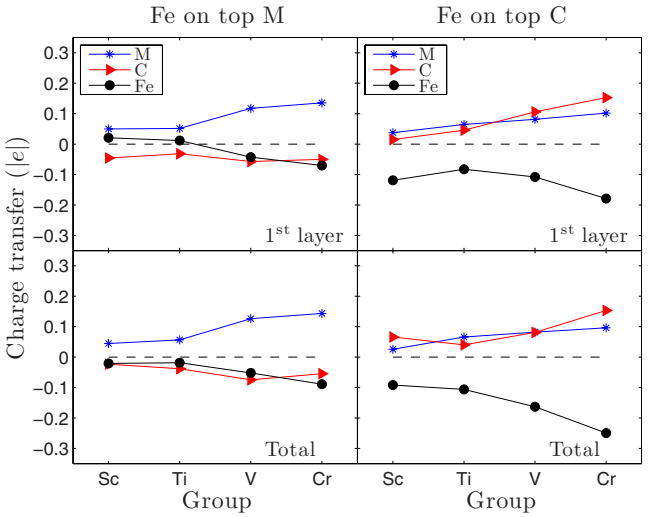

FIG. 10. (Color online) Difference of the Bader charges between the Fe/MC 3*d* interfaces and the corresponding surfaces as a function of the *M* atom. The upper panel shows the charge redistribution for solely the interface layer whereas the lower panel shows the total redistribution in the slabs. Negative (positive) values denote depletion (accumulation).

plained as a combination of the site A and the site B bond mechanisms. The above conclusions are verified to hold for the all the considered Fe/*MX* systems as well and are also in good agreement with previous theoretical works[11–15,18,20] on the Fe/*MX* systems and on other metal-ceramic interfaces.

4. Trends along a period

The increasing bond strength of the interface along a period can be ascribed to the metallic interaction between the Fe and the *M* states in-line with the concept proposed for Co/Ti(C,N) interfaces in Ref. 18. The downwards displacement of the *MX* surface DOS as valence electrons are added shifts the CB closer to the Fe *d* states and thereby increases the energy overlap (cf. Fig. 9). As the interface is created hybridization occurs between the Fe *d* and the *M d* states, which destroys the antibonding character of the partially filled CB. The beneficial interaction increases with the filling of the *M d* states and as a consequence the interface bonds gradually become stronger along a period. The metallic interaction is further supported by a close correlation between the variations in the induced charge density at the A site and the B site and the trends in the work of separation (cf. Figs. 6–8). These variations together with the observed similar trends for all translation states in the interface energy confirm the presence of an overlapping delocalized bond.

5. Trends for carbides vs trends for nitrides

The difference in the trends of the work of separation along a period between the Fe/MC and Fe/MN interfaces that occurs for the Fe/ScC system can be connected to band filling arguments for the *MX* surfaces. The additional *p* electron in the MN's results in the UVB being completely filled from group III and hence the variation in the interface bond strength along a period is determined by the Fe-*M* interaction. In contrast, for the MC's the states in the UVB are first completely occupied from group IV, which leads to that the bonding states in the ScC system are partially empty. As a consequence, the formation of the interface at site B allows for a more beneficial hybridization which compensates for the unfilled bonding states and creates strong bonds between the Fe and the ScC phase. Effectively, the interface strength thus becomes higher than for the remaining Fe/MC 3*d* interfaces. The interaction is supported by the pronounced downwards shift of the LVB and UVB as compared to the surface DOS, which confirms a significant change in the chemical environment, see Fig. 9.

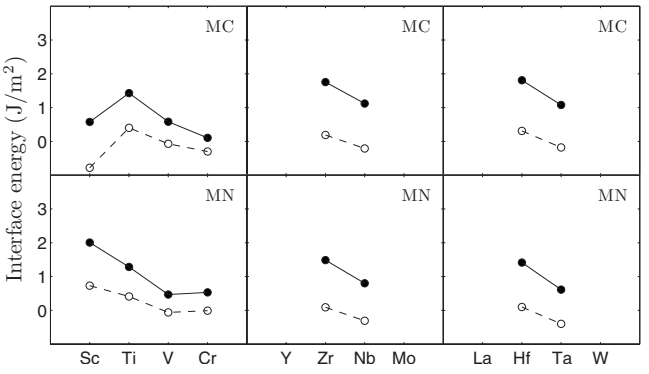

FIG. 11. Variations in the total interface energy (solid lines) for the investigated semicoherent Fe/*MX* interfaces with respect to the *M* atom. The dashed lines correspond to the coherent energies E_{coh}.

C. Semicoherent interface energy

In Fig. 11 we present the semicoherent interface energies for all the considered Fe/*MX* systems. The 1D γ-surface used for the integration in Eq. (5) is constructed from the cut between the coherent B sites (the line *BFC* in Fig. 2). As a comparison we also plot the coherent interface energies E_{coh}. Furthermore, complementary information about the separate chemical and elastic contributions is presented in Fig. 12. It should be noted that we from now on have converted the interface energies from the unit eV/a^2 (which is more appropriate for the analyzes of the chemical bonds as it offers an one-to-one correspondence with the density of states) into the unit J/m^2.

The results in Fig. 11 show that the inclusion of the lattice misfit in the interface description has a substantial impact on the interface energies with contributions ranging up to 1.5 J/m^2. The increased formation cost shifts all the negative interface energies obtained in the coherent limit to positive values. The sign changes have important implications for the stability of *MX* precipitates in Fe, which from a solely interface energy perspective otherwise would decompose into units of a single layer in order to maximize the interface area.

The trends in the semicoherent interface energies are to a large extent found to be preserved from the corresponding trends in the coherent limit. This qualitative resemblance implies that the trends can be understood from the strength of the interface bonds as discussed in the previous subsections. The implication is confirmed by the analysis of the separate

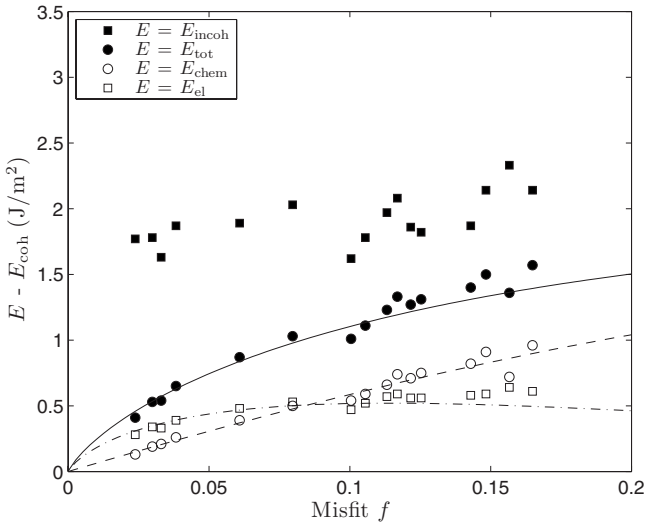

FIG. 12. Calculated interface energies with respect to the coherent energies E_{coh} as a function of the lattice misfit. The solid, the dashed, and the dashed-dotted lines represent an analytical fit (cf. Ref. 36) to the total interface energy, the chemical and the elastic contribution, respectively.

chemical and elastic contributions, where the latter is found to be fairly constant across the investigated range of misfits compared to the former. However, it is important to point out that the mutual relationship between the chemical and elastic contributions changes with the misfit. For small misfit the latter is found to dominate the interface energy whereas for larger misfit closer to the incoherent limit ($f \gtrsim 0.1$) the cost for the chemical distortions constitutes the majority part of the interface energy.

Finally, we find that the above results are in qualitative agreement with the results from an analytical solution (cf. Ref. 36) for an effective medium, obtained by averaging the elastic coefficients and the potential energy surfaces for all the Fe/*MX* systems, see Fig. 12.[76] We can therefore conclude that the elastic and the chemical responses to a specific misfit are close to identical for all the considered interfaces.

D. Stability of the semicoherent interface

Up until this point we have only considered semi-infinite semicoherent Fe/*MX* interfaces. However, in reality finite-sized *MX* precipitates will form in Fe, which consequently can modify the interface energetics. In particular, moderate misfit can alternatively be taken up by coherently strained precipitates.

In order to determine the stability of the semicoherent morphology we consider the coherent interface energetics of thin *MX* films with a thickness h, an infinite extension in the plane parallel to the interface, and with the Baker-Nutting orientation relationship with respect to the Fe lattice. The surrounding Fe phase is assumed to have an infinite extension, and hence, all coherency strains will be taken up by the *MX* film. The coherent interface energy can within a simple continuous model be expressed as (cf. Ref. 36)

TABLE IV. Calculated properties for the coherently strained Fe/MC (Fe/MN) interface systems.

	e_{el} (GPa)	h_c (Å)
Fe/ScX	7.21 (5.73)	3.8 (4.4)
Fe/TiX	3.36 (2.25)	6.1 (7.8)
Fe/VX	1.02 (0.62)	12.7 (17.2)
Fe/CrX	0.31 (0.60)	26.2 (18.1)
Fe/ZrX	11.84 (10.42)	2.6 (2.7)
Fe/NbX	8.77 (6.97)	3.0 (3.2)
Fe/HfX	10.94 (9.15)	2.7 (2.9)
Fe/TaX	9.15 (7.04)	2.7 (2.9)

$$E_{\mathrm{tot}} = E_{\mathrm{chem}} + E_{\mathrm{el}} \approx E_{\mathrm{coh}} + \frac{h}{2} e_{\mathrm{el}}, \tag{12}$$

where e_{el} denotes the elastic energy per volume unit required to strain the *MX* slab. The factor 2 in the denominator is included to account for the presence of two interfaces. We have here assumed that the chemical interactions across the interface can be approximated by E_{coh} obtained from the γ surface evaluation. By equating Eq. (12) with the semicoherent interface energy we can estimate a critical thickness h_c of the *MX* films for which the semicoherent structure becomes stable from energetic arguments, see Table IV.

The results show that strained coherent films of several atomic layers can be stabilized for the 3*d MX* systems before the semicoherent morphology becomes more energetically favorable. For the 4*d* and 5*d MX* films on the other hand the semicoherent structure is expected already when the film thickness exceeds one or two atomic layer(s). However, it should be noted that these results are estimated from the assumption of infinite extension of the film in the plane parallel to the interface. For a finite extension of the films, there is in principle a possibility to simultaneously strain the softer Fe phase together with the stiffer *MX* phase, which would thus reduce the elastic energy required for coherency. It would therefore be plausible to regard our predicted results as lower limits for the critical thickness.

V. CONCLUSIONS

In this work we perform a systematic investigation of the interface energetics of semicoherent Fe/*MX* (X=C,N) interfaces. Our approach is based on an extended Peierls-Nabarro framework, in which *ab initio* DFT data for the chemical interactions across the interface are combined with a continuum treatment to account for the elastic distortions arising from the lattice misfit between the two phases.

The results show that the chemical interactions across the interface depend strongly on the local atomic environment. The Fe on top X configuration is found to be the most energetically stable site with strong bonds comprising aspects of ionic, covalent and metallic character, similar to the bonds in the bulk *MX* systems. In contrast, the weakest bonds occur at the Fe on top *M* site where only minor Fe-*M* interactions are

present. Further, the variations in the strength of the interface bonds along a period are analyzed and discussed within a band filling picture of the bonding and antibonding states of the *MX* phase. Our results show that the variations are mainly determined by the interactions between the Fe *d* states and the antibonding *M d* states. The only exception is found to occur for the Fe/ScC interface where a stronger interaction involving the C states is possible due to unfilled bonding states in the bulk ScC phase.

Furthermore, the energy cost to form the misfit dislocation structure at the semicoherent interface is shown to raise the interface energy significantly (up to 1.5 J/m^2) compared to a coherent interface approximation. For small misfit the elastic contribution from the atomic displacements in the materials is found to dominate the energy cost whereas for larger misfit the chemical contribution from the distortions of the interface bonds is determined to be equally important. Consequently, it is therefore essential to include both the elastic and chemical contributions in the interface model.

Finally, we compare our obtained semicoherent interface energies with estimates for strained coherent thin *MX* films in Fe. From the results we predict that the semicoherent structure is stabilized for all the investigated 4*d* and 5*d MX* systems when the film thickness exceeds one or two atomic layer(s). For the 3*d MX*'s on the other hand strained coherent films of several atomic layers are expected before the transition to the semicoherent structure occurs.

In summary, we have investigated the elastic and chemical contributions to the interface energetics of semicoherent and coherently strained precipitates. The effect of misfit dislocations on the interface energy can be treated within a Peierls-Nabarro framework. The inclusion of the misfit gives a significant contribution to the interface energy and must therefore be accurately accounted for in order to obtain a proper interface description. These findings will have important bearings on our ability to understand the early stage of precipitation and its pathways,[5] to thermodynamically model precipitate stability in Fe-*M*-*X* systems,[77] and to describe long-term microstructural evolution in steels.[78]

ACKNOWLEDGMENTS

This work was supported by the Swedish Foundation for Strategic Research (SSF). The allocations of computer resources at C3SE and the Swedish National Infrastructure for Computing (SNIC) are gratefully acknowledged. The authors wish to thank Hans-Olof Andrén and Sven Johansson for valuable comments.

[1] J. P. Hirth and J. Lothe, *Theory of Dislocations*, 2nd ed. (Wiley, Canada, 1982).
[2] Y. Mishin, M. Asta, and J. Li, Acta Mater. **58**, 1117 (2010).
[3] R. W. K. Honeycombe and H. K. D. H. Bhadeshia, *Steels: Microstructure and Properties*, 2nd ed. (Butterworth–Heinemann, Oxford, UK, 1995).
[4] N. E. Vives Díaz, S. S. Hosmani, R. E. Schacherl, and E. J. Mittemeijer, Acta Mater. **56**, 4137 (2008).
[5] F. Danoix, E. Bémont, P. Maugis, and D. Blavette, Adv. Eng. Mater. **8**, 1202 (2006).
[6] M. Sennour, P. H. Jouneau, and C. Esnouf, J. Mater. Sci. **39**, 4521 (2004).
[7] S. S. Hosmani, R. E. Schacherl, and E. J. Mittemeijer, Acta Mater. **53**, 2069 (2005).
[8] T. C. Bor, A. T. W. Kempen, F. D. Tichelaar, E. J. Mittemeijer, and E. van der Giessen, Philos. Mag. A **82**, 971 (2002).
[9] F.-G. Wei, T. Hara, and K. Tsuzaki, Philos. Mag. **84**, 1735 (2004).
[10] E. Courtois, T. Epicier, and C. Scott, Micron **37**, 492 (2006).
[11] J. Hartford, Phys. Rev. B **61**, 2221 (2000).
[12] A. Arya and E. A. Carter, J. Chem. Phys. **118**, 8982 (2003).
[13] J.-H. Lee, T. Shishidou, Y.-J. Zhao, A. J. Freeman, and G. B. Olson, Philos. Mag. **85**, 3683 (2005).
[14] W.-S. Jung, S.-H. Chung, H.-P. Ha, and J.-Y. Byun, Modell. Simul. Mater. Sci. Eng. **14**, 479 (2006).
[15] S.-H. Chung, H.-P. Ha, W.-S. Jung, and J.-Y. Byun, ISIJ Int. **46**, 1523 (2006).
[16] D. F. Johnson and E. A. Carter, J. Phys. Chem. A **113**, 4367 (2009).
[17] S. V. Dudiy, J. Hartford, and B. I. Lundqvist, Phys. Rev. Lett. **85**, 1898 (2000).
[18] S. V. Dudiy and B. I. Lundqvist, Phys. Rev. B **64**, 045403 (2001).
[19] M. Christensen, S. Dudiy, and G. Wahnström, Phys. Rev. B **65**, 045408 (2002).
[20] S. V. Dudiy and B. I. Lundqvist, Phys. Rev. B **69**, 125421 (2004).
[21] J. Hoekstra and M. Kohyama, Phys. Rev. B **57**, 2334 (1998).
[22] D. J. Siegel, L. G. Hector, and J. B. Adams, Phys. Rev. B **67**, 092105 (2003).
[23] L. M. Liu, S. Q. Wang, and H. Q. Ye, Acta Mater. **52**, 3681 (2004).
[24] R. Benedek, D. N. Seidman, and C. Woodward, J. Phys.: Condens. Matter **14**, 2877 (2002).
[25] R. Benedek, D. N. Seidman, and C. Woodward, Interface Sci. **12**, 57 (2004).
[26] R. Peierls, Proc. Phys. Soc. **52**, 34 (1940).
[27] F. R. N. Nabarro, Proc. Phys. Soc. **59**, 256 (1947).
[28] J. H. van der Merwe, J. Appl. Phys. **34**, 117 (1963).
[29] J. H. van der Merwe and W. A. Jesser, J. Appl. Phys. **63**, 1509 (1988).
[30] Y. Yao, T. Wang, and C. Wang, Phys. Rev. B **59**, 8232 (1999).
[31] Y. Yao and T. C. Wang, Acta Mater. **47**, 3063 (1999).
[32] Y. Zhang and Y. Yao, Eur. Phys. J. B **55**, 355 (2007).
[33] Y. Zhang and Y. Yao, Mod. Phys. Lett. B **22**, 3135 (2008).
[34] N. I. Medvedeva, Y. N. Gornostyrev, O. Y. Kontsevoi, and A. J. Freeman, Acta Mater. **52**, 675 (2004).
[35] S. A. E. Johansson, M. Christensen, and G. Wahnström, Phys. Rev. Lett. **95**, 226108 (2005).
[36] D. H. R. Fors, S. A. E. Johansson, M. V. G. Petisme, and G. Wahnström, Comput. Mater. Sci. **50**, 557 (2010).
[37] W. Weber, P. Roedhammer, L. Pintschovius, W. Reichardt,

F. Gompf, and A. N. Christensen, Phys. Rev. Lett. **43**, 868 (1979).
[38] E. I. Isaev, S. I. Simak, I. A. Abrikosov, R. Ahuja, Yu. Kh. Vekilov, M. I. Katsnelson, A. I. Lichtenstein, and B. Johansson, J. Appl. Phys. **101**, 123519 (2007).
[39] V. I. Ivashchenko, P. E. A. Turchi, and E. I. Olifan, Phys. Rev. B **82**, 054109 (2010).
[40] G. Kresse and J. Hafner, Phys. Rev. B **47**, 558 (1993).
[41] G. Kresse and J. Furthmüller, Comput. Mater. Sci. **6**, 15 (1996).
[42] G. Kresse and J. Furthmüller, Phys. Rev. B **54**, 11169 (1996).
[43] J. P. Perdew, J. A. Chevary, S. H. Vosko, K. A. Jackson, M. R. Pederson, D. J. Singh, and C. Fiolhais, Phys. Rev. B **46**, 6671 (1992).
[44] J. P. Perdew, K. Burke, and M. Ernzerhof, Phys. Rev. Lett. **77**, 3865 (1996).
[45] The use of two different functionals originated from convergence problems for the surface and interface systems with M=Nb,Cr when the PW91 functional was utilized. We have confirmed that the NbX and CrX bulk properties are consistent for the PBE and PW91 functionals. We have also estimated the corresponding effects on the surface and interface energies by employing both the PBE and PW91 functionals in the M=V containing systems. The changes in the surface and interface energies were found to be less than 0.05 J/m^2.
[46] G. Kresse and D. Joubert, Phys. Rev. B **59**, 1758 (1999).
[47] R. F. W. Bader, Chem. Rev. **91**, 893 (1991).
[48] G. Henkelman, A. Arnaldsson, and H. Jònsson, Comput. Mater. Sci. **36**, 354 (2006).
[49] W. R. L. Lambrecht, M. S. Miao, and P. Lukashev, J. Appl. Phys. **97**, 10D306 (2005).
[50] A. Filippetti, W. E. Pickett, and B. M. Klein, Phys. Rev. B **59**, 7043 (1999).
[51] A. Filippetti and W. E. Pickett, Phys. Rev. B **59**, 8397 (1999).
[52] M. J. Mehl, J. E. Osburn, D. A. Papaconstantopoulos, and B. M. Klein, Phys. Rev. B **41**, 10311 (1990).
[53] M. W. Finnis, J. Phys.: Condens. Matter **8**, 5811 (1996).
[54] J. C. Boettger, Phys. Rev. B **49**, 16798 (1994).
[55] V. Fiorentini and M. Methfessel, J. Phys.: Condens. Matter **8**, 6525 (1996).
[56] N. Ridley and H. Stuart, J. Phys. D **1**, 1291 (1968).
[57] P. H. T. Philipsen and E. J. Baerends, Phys. Rev. B **54**, 5326 (1996).
[58] J. Häglund, G. Grimvall, T. Jarlborg, and A. Fernández Guillermet, Phys. Rev. B **43**, 14400 (1991).
[59] H. O. Pierson, *Handbook of Refractory Carbides and Nitrides* (William Andrew/Noyes, New Jersey, 1996).
[60] A. Fernández Guillermet, J. Häglund, and G. Grimvall, Phys. Rev. B **45**, 11557 (1992).
[61] A. Fernández Guillermet, J. Häglund, and G. Grimvall, Phys. Rev. B **48**, 11673 (1993).
[62] X.-J. Chen, V. V. Struzhkin, Z. Wu, M. Somayazulu, J. Qian, S. Kung, A. N. Christensen, Y. Zhao, R. E. Cohen, H.-k. Mao, and R. J. Hemley, Proc. Natl. Acad. Sci. U.S.A. **102**, 3198 (2005).
[63] T. Das, S. Deb, and A. Mookerjee, Physica B **367**, 6 (2005).
[64] A. Vojvodic and C. Ruberto, J. Phys.: Condens. Matter **22**, 375501 (2010).
[65] V. P. Zhukov, V. A. Gubanov, O. Jepsen, N. E. Christensen, and O. K. Andersen, J. Phys. Chem. Solids **49**, 841 (1988).
[66] A. Neckel, P. Rastl, R. Eibler, P. Weinberger, and K. Schwarz, J. Phys. C: Solid State Phys. **9**, 579 (1975).
[67] C. D. Gelatt, A. R. Williams, and V. L. Moruzzi, Phys. Rev. B **27**, 2005 (1983).
[68] A. Fernández Guillermet and G. Grimvall, Phys. Rev. B **40**, 10582 (1989).
[69] J. Häglund, A. Fernández Guillermet, G. Grimvall, and M. Körling, Phys. Rev. B **48**, 11685 (1993).
[70] J. C. Grossman, A. Mizel, M. Côté, M. L. Cohen, and S. G. Louie, Phys. Rev. B **60**, 6343 (1999).
[71] Y. Zhang, J. Li, L. Zhou, and S. Xiang, Solid State Commun. **121**, 411 (2002).
[72] P. Błoński and A. Kiejna, Surf. Sci. **601**, 123 (2007).
[73] H. W. Hugosson, O. Eriksson, U. Jansson, A. V. Ruban, P. Souvatzis, and I. A. Abrikosov, Surf. Sci. **557**, 243 (2004).
[74] F. Viñes, C. Sousa, P. Liu, J. A. Rodriguez, and F. Illas, J. Chem. Phys. **122**, 174709 (2005).
[75] W. Liu, X. Liu, W. T. Zheng, and Q. Jiang, Surf. Sci. **600**, 257 (2006).
[76] The resulting values used in Fig. 12 correspond to $\gamma_{\max}-\gamma_{\min}$ =2.12 J/m^2, $a=a^{\mathrm{Fe}}+A(a^{MX}-a^{\mathrm{Fe}})$ with A=0.70 and a^{Fe} =2.831 Å, and K_e=141 GPa in the notation used in Ref. 36.
[77] M. Perez, E. Courtois, D. Acevedo, T. Epicier, and P. Maugis, Philos. Mag. Lett. **87**, 645 (2007).
[78] J. Hald, Int. J. Pressure Vessels Piping **85**, 30 (2008).